

Full Reaction Pathway Dynamics for Atmospheric Decomposition Reactions: The Photodissociation of H_2COO

Cangtao Yin and Markus Meuwly*

Department of Chemistry, University of Basel, Klingelbergstrasse 80, CH-4056 Basel, Switzerland.

E-mail: m.meuwly@unibas.ch

Abstract

Branching ratios for fragmentation channels of important meta- and unstable species are essential for a molecular-level characterization of atmospheric chemistry. Here, the molecular product channels for the decomposition dynamics of the smallest Criegee intermediate, H_2COO , are quantitatively investigated. Using a high-quality, full-dimensional machine learned potential energy surface (CASPT2/aug-cc-pVTZ), the translational, rotational, and vibrational energy distributions of the $\text{CO}_2 + \text{H}_2$, $\text{H}_2\text{O} + \text{CO}$, and $\text{HCO} + \text{OH}$ fragmentation channels were analyzed to elucidate partitioning of the available energy. The $\text{CO}_2 + \text{H}_2$ product forms through two different pathways that bifurcate after formation of the OCH_2O intermediate. Along the direct pathway, CO_2 is preferentially vibrationally excited with H_2 in its vibrational ground state, whereas for the indirect pathway going through formic acid, H_2 can populate levels with $v > 0$. For all product channels passing through energized formic acid, the lifetime distributions are described by stretched exponentials with β ranging from 1.1 to 1.7. This is a clear signature of non-RRKM effects and suggests that the explicit molecular dynamics needs to be followed for a quantitative and realistic description of the photodissociation dynamics.

Keywords: Energy transfer; Machine Learning; Molecular dynamics; Nonequilibrium processes; Stretched Exponentials

Criegee intermediates,¹ formed through ozonolysis of alkenes, are central species for the chemical evolution of Earth's atmosphere. Their formation route $\text{R}_1\text{R}_2\text{C}=\text{CR}_3\text{R}_4 + \text{O}_3 \rightarrow \text{R}_1\text{R}_2\text{COO} + \text{R}_3\text{R}_4\text{C}=\text{O}$ implies that they are generated with considerable, but largely unknown amounts of internal energy. Previous calculations on the $\text{O}_3 + \text{C}_2\text{H}_4$ cycloaddition reaction report a gain of -48.1 kcal/mol of the $\text{H}_2\text{COO} + \text{CH}_2\text{O}$ product relative to the reactants.² CIs are chemically unstable. They either decay through unimolecular (photo)dissociation³⁻⁵

or react with other compounds including SO_2 , NO_2 , or H_2O in the atmosphere.^{6–10} Their relevance for atmospheric chemistry lies in providing a fast, non-photolytic conversion of ethene and ozone into stable end products, including a prompt source of molecular hydrogen H_2 .¹¹ Although the lifetime of the smallest Criegee intermediate, H_2COO , is rather short (seconds to sub-seconds, depending on humidity),^{12,13} the global ubiquity of ethene ozonolysis implies that H_2COO contributes measurably to the tropospheric H_2 budget and influences the closure of carbon oxidation pathways.¹⁴ Furthermore, H_2COO serves as a benchmark system for characterizing energy disposal and unimolecular reaction dynamics in Criegee intermediates more generally. Consequently, a quantitative characterization of the molecular decomposition pathways of H_2COO is of great general interest.

Compared with H_2COO , the unimolecular decay of the next-larger CI, *syn*- CH_3CHOO , has been studied extensively in both experiments^{15,16} and theory.^{17,18} This is partly because the rate of OH formation from *syn*- CH_3CHOO is much higher than for H_2COO , which facilitates its laboratory experimental detection. Analysis of the product translational energy release for *syn*- CH_3CHOO revealed¹⁸ that a quantitative interpretation of the experimental observations requires tracking the full reaction evolution, from the initial non-equilibrium preparation of the reactant through intermediates to the final products.¹⁹ Starting reactive molecular dynamics (MD) simulations from intermediates or transition states along the decomposition pathway provided qualitative but not quantitative information about the final state distributions.¹⁹

The present work aims at characterizing in a quantitative fashion the end-to-end reaction dynamics of H_2COO , with a particular focus on the analysis of final product states and bifurcating dynamics. To achieve this, additional reference data in the product regions was included into the training of the previously developed global potential energy surface (PES).²⁰ This yields a suitably extended and improved machine learning-based PES (ML-PES)

for final state analysis based on CASPT2 reference data, which provides an accurate and unified description of all possible reaction channels. The improved coverage of the product regions ensures a reliable representation of bond breaking and formation processes and allows long-time trajectory propagation.

The performance of the trained ML-PESs was evaluated by comparing NN-predicted energies E and forces F with reference CASPT2 calculations, see Figure S1. Specifically, the mean absolute (MAE) and root mean squared errors (RMSE) were computed for both quantities using a test set of approximately 1500 structures. For the best-performing PhysNet model, the $\text{MAE}(E)$ and $\text{RMSE}(E)$ are 1.23 kcal/mol and 2.14 kcal/mol, respectively. The corresponding errors for forces are $\text{MAE}(F) = 1.11 \text{ kcal/mol}/\text{\AA}$ and $\text{RMSE}(F) = 3.80 \text{ kcal/mol}/\text{\AA}$. Remarkably, the data set spans $\sim 150 \text{ kcal/mol}$, as shown in Figure 1. Furthermore, the model shows a very high correlation with the reference data, with $R^2 = 0.9984$, demonstrating that it accurately reproduces the trends and variations in the CASPT2 energies. The performance of the present model is comparable in accuracy to previously reported results,^{18,20,21} indicating that the ML-PES maintains the reliability of earlier models while extending their applicability to the dissociation products.

For the three molecular product channels, 1- and 2-dimensional PESs are reported in Figures S2 to S5. For the product diatomics H_2 , CO , and OH , all 1-d curves are globally smooth and well-behaved which is notable because the full-dimensional PES is trained as a whole. Also, the energy profiles only depend moderately on the separation d away from the respective triatomic interaction partner. At large diatom–triatom separations ($d \sim 5 \text{ \AA}$, blue traces in Figure S2), the intermolecular interactions decrease to a degree that the energy profiles approach those of the isolated di- and triatomic species. In the asymptotic limit, a crossing appears for the $\text{HCO} + \text{OH}$ channel. However, this feature occurs at energies well above the initial energy of the simulations (approximately 25.5 kcal/mol) and therefore does not

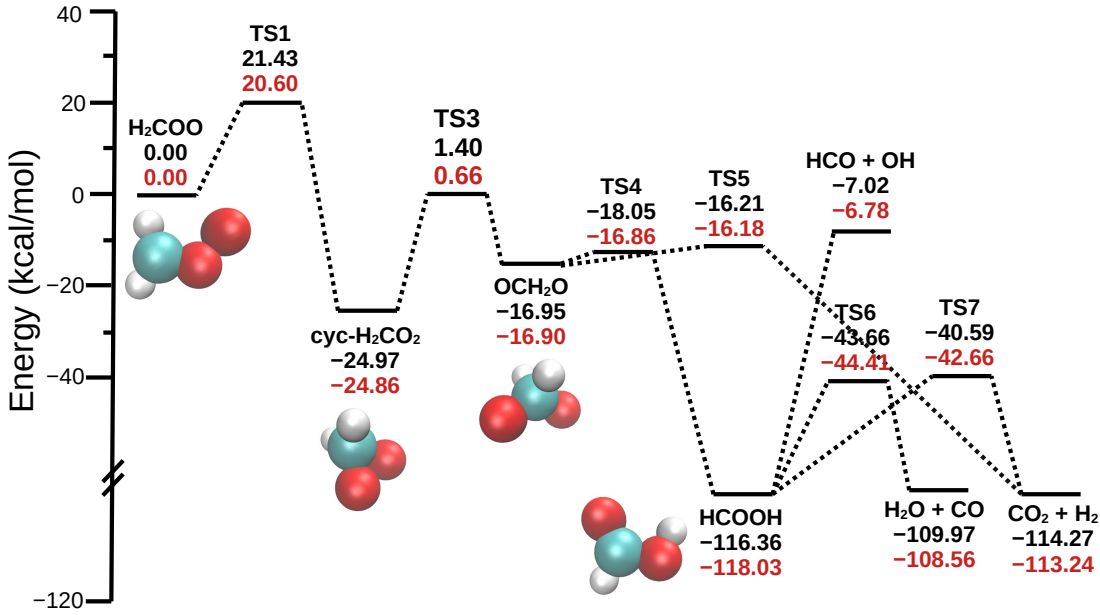


Figure 1: The unimolecular decomposition of H_2COO into three bimolecular products: $\text{CO}_2 + \text{H}_2$, $\text{H}_2\text{O} + \text{CO}$, and $\text{HCO} + \text{OH}$. The formation of $\text{CO}_2 + \text{H}_2$ proceeds through two competing pathways: the “direct pathway”, which connects OCH_2O directly to the products via TS5 , and the “indirect pathway”, in which OCH_2O first isomerizes to HCOOH (formic acid) before forming $\text{CO}_2 + \text{H}_2$.

influence the MD trajectories, considering that the initial energy of simulation is around 25.5 kcal/mol.

Figures S3 to S5 illustrate the PESs of the triatomic products CO_2 , H_2O , and HCO in the presence of their corresponding diatomic partners, H_2 , CO , and OH , respectively. Again, all PESs are smooth and well-behaved which allow to run valid reactive MD simulations and to analyze the vibrational contribution to the total internal energy of the fragments. For CO_2 and short intramolecular separation ($d = 1.70 \text{ \AA}$, see Figure S3A) the energy profile of two CO bond stretching is not symmetric with respect to the diagonal, since the interaction between CO_2 and H_2 breaks this symmetry. With increasing d the expected symmetry of $V(r_{\text{CO}_A}, r_{\text{CO}_B})$ becomes apparent. The C–O dissociation energy for the oxygen atom away from CO_2 from the NN-PES is ~ 130 kcal/mol which agrees favourably with the experimentally reported value of 126 kcal/mol.²² This supports the reliability of the

present PES. For $\text{CO}_2 + \text{H}_2$, the CO bonds remain intact because dissociation requires much higher energy and in the MD trajectories some energy is carried away by H_2 , making CO bond cleavage unlikely. For the $\text{H}_2\text{O} + \text{CO}$ system (see Figure S4, variations in the OH bond lengths are similarly explored across different $\text{H}_2\text{O}-\text{CO}$ separations, revealing a stable triatomic product region under the simulation conditions.

For $\text{HCO} + \text{OH}$, the potential energy minimum rises with increasing $\text{HCO}-\text{OH}$ separation, consistent with the endothermic character of HCOOH decomposition. For the HCO triatomic, the CH bond dissociation energy from the present NN-PES is ~ 15 kcal/mol. This compares well with earlier measurements which reported values of [13.36, 14.40, 14.54] kcal/mol and validates this 3d-PES.²³⁻²⁵ In addition, along the H-atom dissociation pathway, a transition state is observed in this figure. This transition state was also identified in earlier MRCI/aug-cc-pVQZ²³ and CCSD(T)/CBS//CCSD/aug-cc-pVTZ²⁴ studies and lies below the initial 25.5 kcal/mol of energy available in the MD simulations. As a result, a small fraction of trajectories proceeded to form the $\text{H} + \text{CO} + \text{OH}$ products. The minimum rises with increasing $d(\text{HCO}, \text{OH})$, in contrast to the CO_2+H_2 and $\text{H}_2\text{O}+\text{CO}$ cases. This behavior is expected, as HCOOH decomposition along this pathway proceeds without a transition state.

Following previous experimental^{19,26} and computational^{17,18,20,21} work, the reactant H_2COO was energized through selective vibrational excitation (see Methods). Such an excitation scheme mimics energy localization in specific internal modes and allows the system to efficiently access the reactive regions of the PES. As a result, the full unimolecular decay of H_2COO can be followed dynamically, enabling a direct examination of the reactions and the associated nonequilibrium dynamical effects governing product formation. In particular, the translational, rotational and vibrational energies characterizing each fragment can be analyzed and compared, see Methods. Intermediate structures sampled along the reaction pathways are identified through geometrical criteria summarized in Table S1

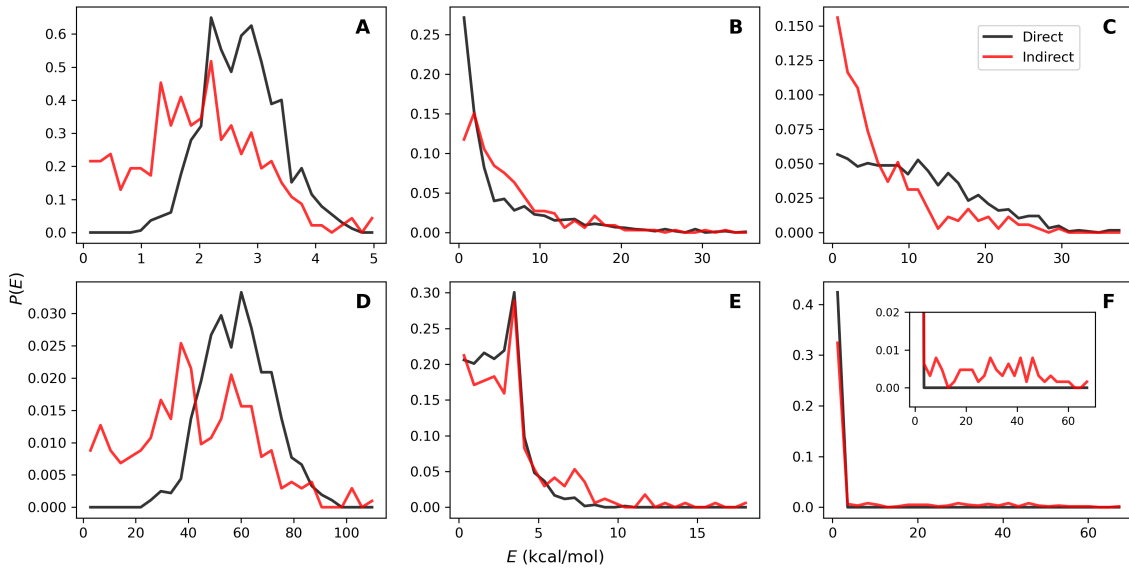


Figure 2: Energy distributions for the $\text{CO}_2 + \text{H}_2$ product channel. Trajectories follow direct (952) and indirect (268) routes. Top panels: fragment CO_2 ; bottom panels: fragment H_2 . From left to right: translational, rotational, and vibrational energy distributions. The inset in panel F indicates that $v > 0$ can be populated for H_2 along the indirect pathway. Note the different scales along the x -axes for panels A-C vs. D-F.

Product State Analysis: With validated product state potential energy surfaces, a total of 4000 nonequilibrium ML-MD simulations was run (see Methods): 952 and 268 formed $\text{CO}_2 + \text{H}_2$ directly and indirectly through HCOOH , respectively, 664 formed $\text{H}_2\text{O} + \text{CO}$, and 40 formed $\text{HCO} + \text{OH}$. The remaining trajectories do not progress beyond the reactant and decay on longer time scales. The energy distributions of the final products were analyzed separately for each of the 4 identified pathways. Formation of $\text{CO}_2 + \text{H}_2$ (Figure 2) along the direct (black traces) pathway yields Gaussian-shaped translational energy distributions for CO_2 (panel A) and H_2 (panel D), with H_2 acquiring particularly high translational energies due to its low mass. For the indirect pathway (red traces in panels A and D) the shapes of $P(E_{\text{trans}})$ deviate from a Gaussian and it is noted that E_{trans} is generally higher along the direct pathway compared to the indirect pathway.

The rotational energy distributions are comparable for both pathways, see Figures 2B/E.

Evidently, $P(E_{\text{rot}})$ for H_2 is not in thermal equilibrium, but given the large rotational constant of H_2 ($B = 61 \text{ cm}^{-1}$) only $j = 0$ and potentially $j = 1$ are expected to be populated. In contrast, the vibrational energy shows a distinct difference: CO_2 (panel C) gains more energy along the direct pathway, whereas for H_2 (panel F) the vibrational degree of freedom contains sufficient energy along the indirect pathway to excite states with $v > 0$ given that the fundamental $\text{H}_2(v = 1)$ appears at 4400 cm^{-1} , corresponding to $\sim 12.6 \text{ kcal/mol}$. This is also an experimentally accessible quantity which allows to distinguish the two pathways.

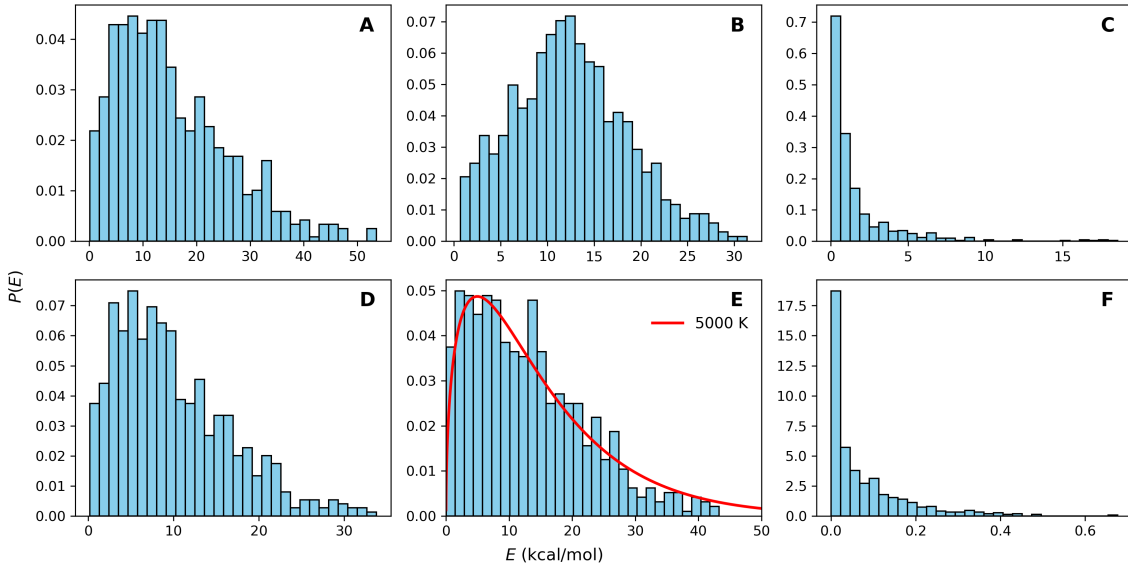


Figure 3: Energy distributions of the product $\text{H}_2\text{O} + \text{CO}$ from 664 simulations. The top panels show fragment H_2O and bottom show fragment CO . From left to right, the distributions correspond to translational, rotational, and vibrational energies. The red trace in panel E corresponds to a Boltzmann distribution with $T = 5000 \text{ K}$ and suggests that the rotational motion of dissociating CO is close to thermal equilibrium.

For the $\text{H}_2\text{O} + \text{CO}$ channel, the energy partitioning into translational, rotational, and vibrational contributions is shown in Figure 3. The CO product remains exclusively in the vibrational ground state (panel F) as $\sim 6 \text{ kcal/mol}$ (2143 cm^{-1}) is required to reach $v = 1$. For H_2O , on the other hand, $P(v)$ extends out to $\sim 20 \text{ kcal/mol}$ which suffices to populate vibrational levels: the 3 fundamental vibrations (1595 , and 3657 to 3756 cm^{-1}) require 4.6 and 10.5 to 11.0 kcal/mol for populating the bending and stretching modes,

respectively. For CO, the Boltzmann distribution $P(j) = \exp[-\beta E_{\text{rot}}(j)]$ for $T = 5000$ K and with $E_{\text{rot}} = Bj(j + 1)$ where $B = 1.93 \text{ cm}^{-1}$ closely follows the histogram which indicates that the product diatomic is close to rotational equilibrium. However, there is also a “plateau” in $P(E_{\text{rot}}^{\text{CO}})$ at low rotational energies which is reminiscent of that seen for OH-dissociation from vibrationally excited *syn*-CH₃CHO. In that case a plateau spanning rotational quantum numbers from 3 to 6 was observed in both, experiment¹⁹ and simulations.¹⁸

Finally, for HCO + OH (Figure S6), the final state distributions are not sufficiently well-converged because only 40 trajectories contribute to this fragmentation channel. Nevertheless, it is evident, that the translational energies are considerably smaller ($E_{\text{trans}}^{\text{HCO}} \lesssim 7 \text{ kcal/mol}$ and $E_{\text{trans}}^{\text{OH}} \lesssim 10 \text{ kcal/mol}$) than for the other two pathways. The vibrational energies ($E_{\text{vib}}^{\text{HCO}} \lesssim 6 \text{ kcal/mol}$ and $E_{\text{vib}}^{\text{OH}} \lesssim 0.025 \text{ kcal/mol}$) only suffice to excite the HCO bending and CO local modes (1101 cm^{-1} and 1870 cm^{-1} , equivalent to 3.1 kcal/mol and 5.3 kcal/mol), but not the CH and OH stretch modes (2750 and 3737 cm^{-1} , corresponding to 7.9 and 10.7 kcal/mol). The only notable excitations are for the rotational degrees of freedom, for which $\sim 10 \text{ kcal/mol}$ are available for both reaction products.

Bifurcating Pathway to yield CO₂ + H₂: As noted earlier, formation of CO₂ + H₂ can follow two competing pathways. With an initial energy content of 25.5 kcal/mol in the reactant (H₂COO), the excess energy in OCH₂O is $> 40 \text{ kcal/mol}$. Hence, OCH₂O is unstable (lifetime $< 0.1 \text{ ps}$) and the reaction pathway towards CO₂+H₂ bifurcates into a direct and an indirect route through a formic acid (HCOOH) intermediate, see Figure 1.

Notably, the OCH₂O lifetime distributions for the direct (black) and indirect (red) pathways differ substantially, see Figure 4. The distribution for the direct pathway is shifted toward longer times, with a peak at approximately 60 fs, whereas the indirect pathway exhibits a maximum at $\sim 30 \text{ fs}$. Indeed, the configurational energy distributions of the OCH₂O

intermediate from trajectories following the direct (black) and indirect (red) pathways reflect the differences in the lifetimes: along the direct pathway the maximum of $P(E_{\text{int}})$ (centered around 0) is shifted towards lower energies than for the indirect pathway (peak at 5 kcal/mol) which extends the lifetime for this intermediate and their median values (dashed lines) differ by 2.2 kcal/mol. Other than that, the two energy distributions are comparable in terms of their shape.

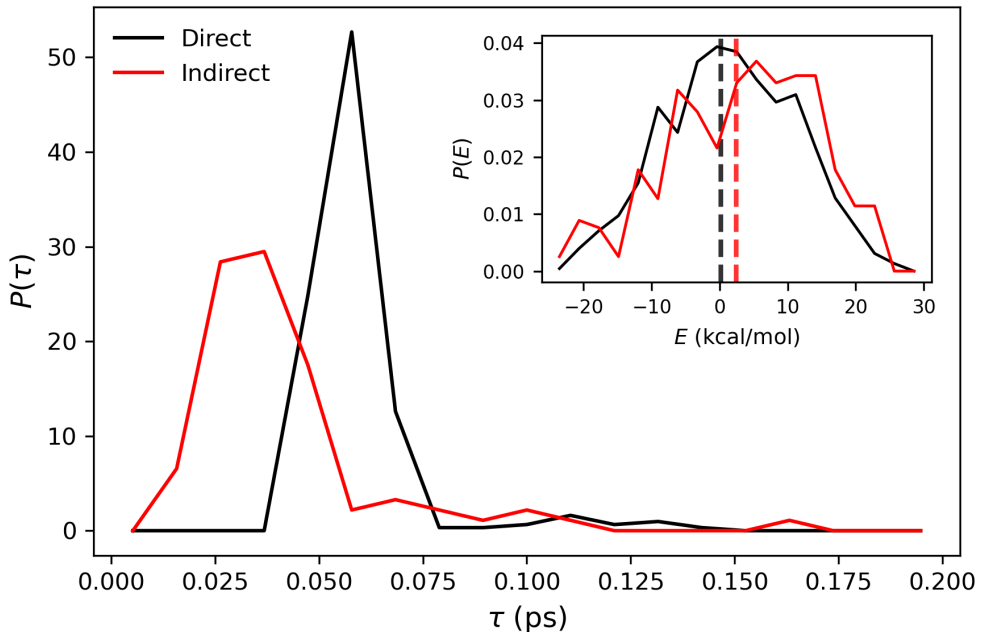


Figure 4: Lifetime (main view) and energy (inset) distributions of OCH_2O for the direct (black) and indirect (red) channels. In both cases, OCH_2O is short-lived, with lifetimes never exceeding 0.2 ps. In the inset, the median energy (dashed vertical lines) are at 0.2 and 2.4 kcal/mol, for the direct and indirect cases, respectively.

The differences between the two pathways become even more evident when analyzing structural properties. Figure 5 reports the $P(r_{\text{CH}}, \theta_{\text{HCH}})$ distribution relating the shorter of the two CH bond lengths with the H-C-H bond angle in OCH_2O . For the direct pathway, the H-C-H angle distribution extends to significantly smaller values (40°), and the CH bond length stretches considerably more away from the equilibrium structure. These two motions are required for (direct) H_2 formation. In contrast, the indirect pathway exhibits a C-H bond

length distribution shifted toward shorter values. This trend is consistent with the fact that the C–H bond length in HCOOH (1.09 Å) is shorter than that in OCH₂O (1.12 Å). Together, these differences in the joint geometric distributions highlight that the reaction outcome is closely linked to the instantaneous molecular geometry, reinforcing the picture that molecular motion rather than total energy alone, plays a key role in steering the reaction pathways.

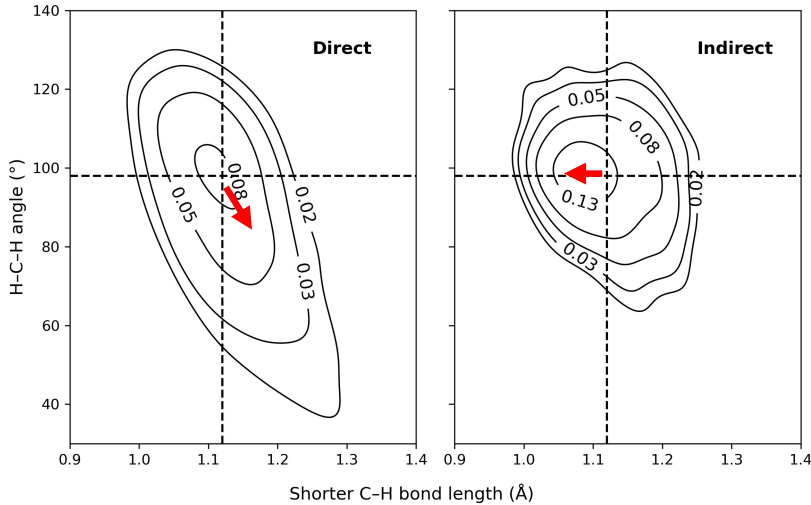


Figure 5: Normalized probability distributions $P(r_{CH}, \theta_{HCH})$ while sampling the OCH₂O well for each of the direct (left) and indirect (right) channels. The numbers in the contour lines indicate the normalized intensity of geometries. The dashed lines represent the equilibrium structure of OCH₂O, and the geometrical criteria used to assign sampled structures to each product channel are listed in Table S1. The red arrows illustrate the reaction pathways from OCH₂O to the corresponding reaction pathways.

Breakup Dynamics of Unstable HCOOH: With an excess energy of ~ 140 kcal/mol, HCOOH formed through nonequilibrium preparation of the reactant is highly unstable, in particular with respect to the two lower-lying product channels CO₂+H₂ and H₂O+CO, see Figure 1. The energy distributions of HCOOH associated with the three product channels, HCO+OH, H₂O+CO, and CO₂+H₂, are similar, see Figure S7. This behavior serves as a useful sanity check, as no clear distinctions are observed in either the overall shape or the accessible energy range. It confirms that the total internal energy of HCOOH alone does not play a decisive role in determining the subsequent reaction outcome. This suggests

that the branching into different product channels is not governed by energy selection alone, but instead arises from dynamical effects such as mode specific energy flow and structure evolution. The similarity of the energy distributions further supports the conclusion that HCOOH dissociates under strongly nonequilibrium conditions, where the instantaneous configuration and dynamics of the intermediate, rather than its total energy, control reaction pathway selection.

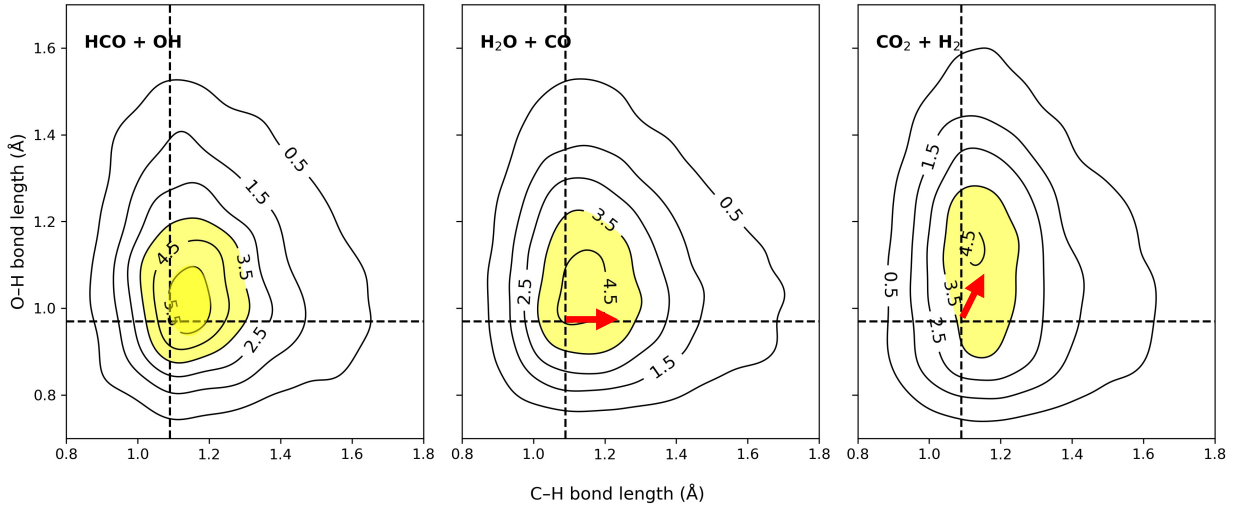


Figure 6: Normalized probability distributions $P(r_{\text{CH}}, r_{\text{OH}})$ sampled in the HCOOH well for the three product channels: $\text{HCO} + \text{OH}$ (left), $\text{H}_2\text{O} + \text{CO}$ (middle), and $\text{CO}_2 + \text{H}_2$ (right). The dashed lines indicate the equilibrium geometry of HCOOH, and the geometrical criteria used to assign sampled structures to each product channel are listed in Table S1. The numbers on the contours denote the normalized population density. Red arrows in the middle and right panels illustrate the reaction pathways from HCOOH to the corresponding products.

Figure 6 shows the joint distributions $P(r_{\text{CH}}, r_{\text{OH}})$ relating the OH and CH bond lengths in HCOOH. For trajectories leading to $\text{HCO} + \text{OH}$ (left panel), the distribution is strongly localized near the equilibrium geometry of formic acid, with CH and OH bond lengths close to 1.09 Å and 0.97 Å, respectively, which are close to the equilibrium bond lengths in the HCO and OH fragments. This allows dissociation to occur without substantial distortion of the HCO and OH subunits within the HCOOH molecule. In contrast, trajectories that produce

$\text{CO}_2 + \text{H}_2$ (right panel) exhibit systematically elongated O–H bond lengths: the maximum of $P(r_{\text{CH}}, r_{\text{OH}})$ is at $r_{\text{OH}} = 1.15 \text{ \AA}$, considerably away from the equilibrium structure (dashed horizontal line). This reflects the progressive cleavage of the OH bond along this reaction pathway. The broader spread of geometries in this region highlights the role of specific bond elongation in steering the system toward different products. Compared to the $\text{CO}_2 + \text{H}_2$ channel (right panel), the $\text{H}_2\text{O} + \text{CO}$ channel (middle panel) exhibits pronounced C–H bond stretching but no O–H bond stretching. This behavior is expected, as formation of $\text{H}_2\text{O} + \text{CO}$ requires cleavage of the C–H bond, whereas the O–H bond remains intact, as indicated by the red arrows illustrating the reaction directions. Together, these geometric distributions demonstrate that product branching is closely tied to the instantaneous molecular structure of HCOOH rather than to its total internal energy, reinforcing the picture of a dynamically controlled bifurcation.

The three product channels also differ in the H–H separations that are sampled when leaving the distribution of FA-geometries. Figure S8 shows the time evolution of the H–H separation along the three pathways for five representative reactive MD trajectories each. The zero of time is shifted so that $t = 0$ corresponds to the frame at which products start to be formed (see Table S1). While still in the well of HCOOH, the H–H distance fluctuates around 2.79 \AA , consistent with the equilibrium H–H separation in HCOOH. As the reaction proceeds, distinct behaviors emerge for each channel. For trajectories forming $\text{HCO}+\text{OH}$ (black), the H–H distance increases sharply near $t = 0$, reflecting the separation of the two fragments. In contrast, trajectories yielding $\text{H}_2\text{O}+\text{CO}$ (red) show stabilization of the H–H distance around 1.52 \AA , characteristic of the equilibrium geometry of water, whereas those producing CO_2+H_2 (blue) exhibit fluctuations around 0.74 \AA , corresponding to the H–H equilibrium bond length in H_2 .

The most profound difference between the three reaction channels emerging from energized HCOOH is found for the lifetime distribution $P(\tau)$ of HCOOH before breakup, see Figure 7.

To characterize these distributions quantitatively, they were fitted to stretched exponential functions $P(\tau) = e^{-(\tau/\tau_c)^\beta}$, with τ the lifetime and τ_c the characteristic time scale on which $P(\tau)$ decays. The use of stretched-exponential kinetics was originally motivated by empirical observations that relaxation and decay processes could not be adequately described by finite sums of exponentials over extended time windows.^{27,28} Subsequently, it was recognized that the stretched exponential provides a compact and robust representation of relaxation arising from a broad, continuous distribution of timescales or energy barriers.^{29–31} While also offering a parameter-efficient alternative to multi-exponential fits, its primary value lies in encoding physical heterogeneity through the stretch exponent β rather than in minimizing the number of fit parameters.

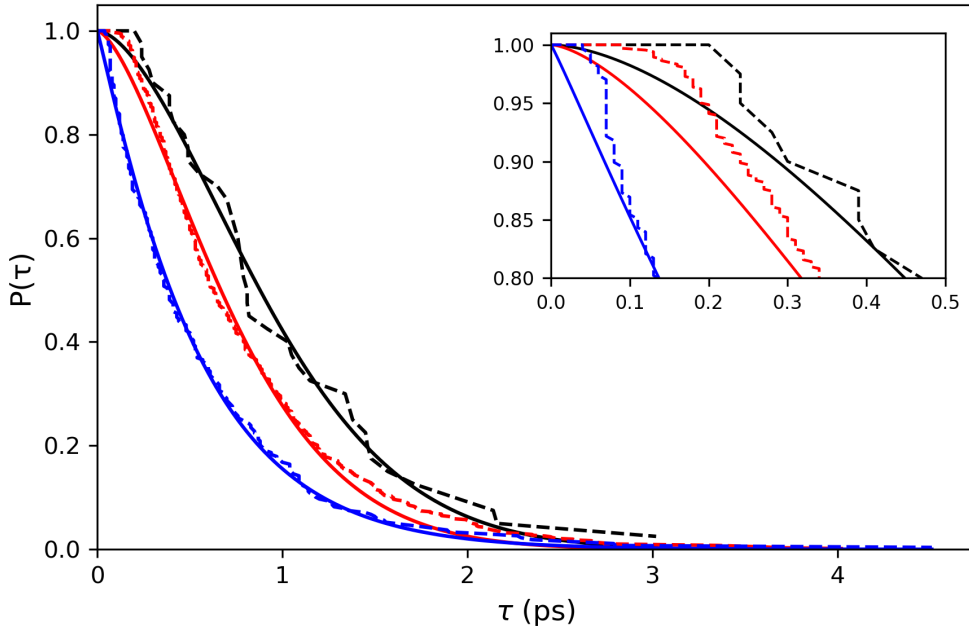


Figure 7: Lifetime distributions of HCOOH associated with the three product channels HCO+OH (black), H₂O+CO (red), and CO₂+H₂ (blue). The dashed lines represent the raw data, while solid lines show the fits using a stretched exponential function, $P(\tau) = \exp [-(\tau/\tau_c)^\beta]$, with $\tau_c = 1.1; 0.8; 0.6$ ps and $\beta = 1.7; 1.5; 1.1$ for the HCO+OH; H₂O+CO; CO₂+H₂ pathways, respectively. The inset shows a magnified view of the early-time decay of the survival probability. Notably, for all three pathways there is a finite lifetime ranging from 75 fs to 200 fs during which no product is formed. Depending on the product channel considered, this HCOOH-lifetime differs by a factor of 3.

The raw survival curves show a short-time plateau preceding the onset of decay, which can be interpreted as an apparent initialization time. During this early period, trajectories remain in the reactant region and do not immediately lead to product formation. The extent of this plateau varies among the reaction channels: the HCO+OH channel (black) exhibits the longest delay, while the CO₂+H₂ channel displays the shortest. Although the precise origin of this behavior cannot be uniquely determined from the present data, the observed channel dependence suggests that different preparatory intramolecular motions or structural fluctuations may be required before the system can access the corresponding dissociation pathways.

In the present case, the fitted parameters $[\beta, \tau_c]$ differ considerably for the three product channels. This is particularly apparent for the stretch exponent β . A stretch exponent $\beta \sim 1$ indicates near single-exponential decay, consistent with statistical unimolecular kinetics in the RRKM limit, whereas $\beta > 1$ points towards compressed-exponential behaviour which is not associated with statistical unimolecular kinetics. On the other hand, $0 < \beta < 1$ points towards dynamic heterogeneity, traps, or rough energy landscapes as they appear for glasses,³² for proteins,^{33,34} or for diffusion on rough surfaces such as amorphous solid water.³⁵ In the present case, clearly all values $\beta > 1$. For CO₂+H₂, $\beta = 1.1$ which is closest to RRKR-like dynamics whereas for the the H₂O+CO and HCO+OH channels $\beta = 1.5$ and $\beta = 1.7$, respectively, which is evidently non-RRKM. Remarkably, Figure 4 does not report any difference between the three pathways, whereas the HCOOH lifetime distribution $P(\tau)$ allows to distinguish them and provides deeper physical insights. One slight caveat concerns the HCO+OH channel for which only 40 events are available, whereas for the two lower-lying product channels statistically significant numbers of trajectories have been analyzed. Nevertheless, the conclusion from this analysis remains that non-RRKM dynamics is found for all three channels.

Overall, the present work found non-RRKM dynamics for all three molecular fragmentation

channels for the unimolecular decay of vibrationally excited H_2COO . For the H_2 -production channel, $\beta = 1.7$ is largest which points towards pronounced non-RRKM characteristics of this decay pathway going through formic acid. Also, the product H_2 generated along this pathway is in thermal nonequilibrium and can populate vibrationally excited states of the diatomic, see red trace Figure 2F. For the direct route, H_2 remains in its vibrational ground state which provides a way to distinguish the two pathways in experiments.

Analysis of joint probability distributions of internal coordinates clarifies their role in selecting a particular reaction pathways. For the bifurcating reaction, $P(r_{\text{CH}}, \theta_{\text{HCH}})$ in Figure 5, clearly distinguishes between the direct and the indirect pathway for $\text{CO}_2 + \text{H}_2$ formation. Likewise, $P(r_{\text{CH}}, r_{\text{OH}})$ provides a molecular-level understanding for the differences between the three product channels emanating from energized HCOOH .

In conclusion, this study provides a mechanistic and quantitative picture for the photodissociation dynamics of energized H_2COO under near-laboratory conditions.^{19,26} Together with earlier work on *syn*-Criegee, it is found that statistically significant numbers of trajectories on ML-trained PESs at the CASPT2 level of theory provide a meaningful starting point for molecular-level exploration of these important and challenging systems.^{18,20} Concerning the important role of H_2COO to contribute measurably to the tropospheric H_2 budget, it was explicitly shown that H_2 can be formed exclusively in the ground vibrational state (direct) or populate vibrationally excited states for the reaction along the indirect route through formic acid. Finally, it is demonstrated, that non-RRKM dynamics is at play which underlines the importance of dynamical simulations for understanding complex, multichannel reactions that cannot be fully described by kinetic studies alone.

Supporting Information

The supporting information describes the Methods (training of PhysNet, MD simulations, energy decomposition analysis) and provides additional information about the product state PESs together with figures and tables.

Data Availability

The reference data that allow to reproduce the findings of this study are openly available at

Acknowledgment

Financial support from the Swiss National Science Foundation through grants 200020_219779 (MM), 200021_215088 (MM), the University of Basel (MM) is gratefully acknowledged. This article is based upon work within COST Action COSY CA21101, supported by COST (European Cooperation in Science and Technology) (to MM).

SUPPORTING INFORMATION: Full Reaction Pathway Dynamics for Atmospheric Decomposition Reactions: The Photodissociation of H₂COO

S1 Methods

S1.1 Construction of ML-PES

To achieve a faithful description of the full reactive landscape connecting H₂COO to its bimolecular products CO₂+H₂, H₂O+CO, and HCO+OH, the ML-PES employed in this study was refined by augmenting an existing data set with additional reference points in the product regions.²⁰ This extended data coverage is a prerequisite and essential for an adequate description of the asymptotic behavior of each product channel and for ensuring smooth and stable trajectory propagation throughout the dissociation processes in the ML-MD.

All electronic structure calculations used to generate the reference energies were performed at the CASPT2/aug-cc-pVTZ (CASPT2/aVTZ), using the MOLPRO program package.³⁶ The underlying complete active space self-consistent field (CASSCF) calculations were carried out using an active space comprising 12 electrons distributed among 11 orbitals - i.e. CASSCF(12,11) - which provides a balanced description of the multireference character along the reaction pathways.

Starting from the existing 13877 geometries,²⁰ random displacements were applied to generate 1053 additional structures in the three product regions (CO₂+H₂, H₂O+CO, and HCO+OH), excluding configurations with energies more than 150 kcal/mol above the optimized H₂COO. The resulting data set, combined with the original structures, comprised a total of 14930 geometries.

ML-PESs were trained using the PhysNet³⁷ NN architecture and an 80/10/10 split of the

reference data set into training, validation, and test subsets. Four independent NN-PESs were trained, and the model with the smallest $MAE(E)$ was selected for the subsequent ML-MD simulations.

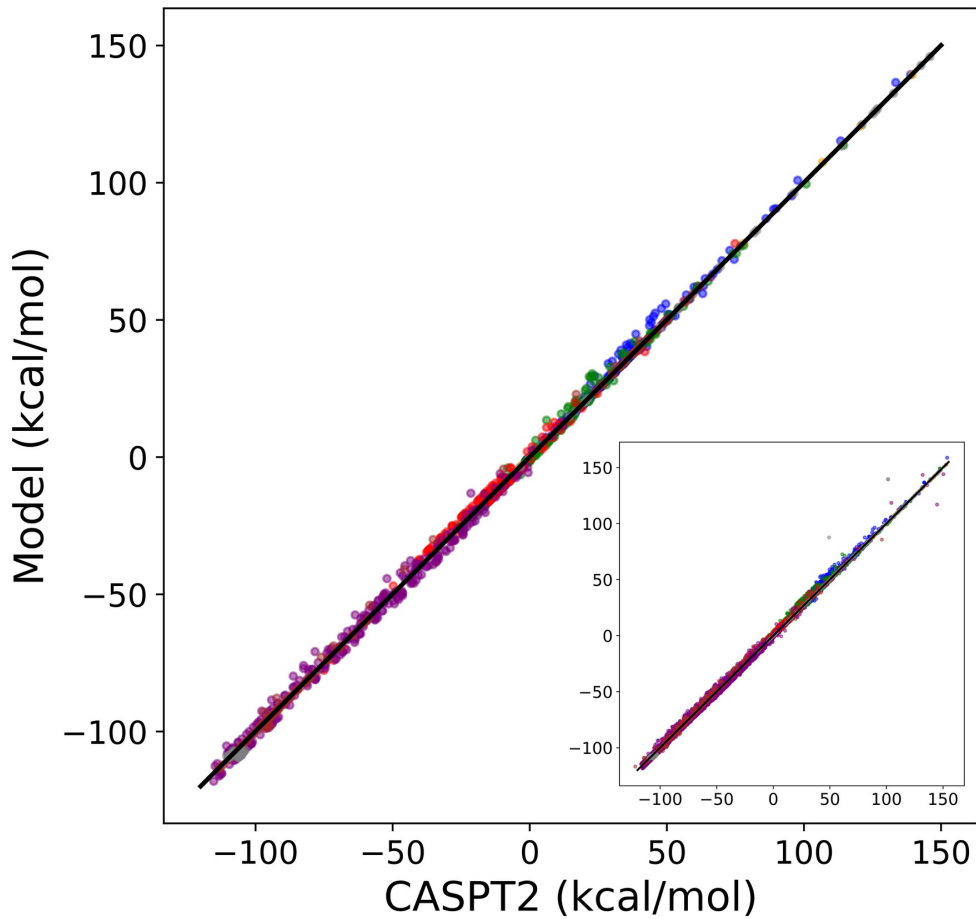


Figure S1: Relationship between the CASPT2/aVTZ reference energies and the model predictions. The main panel shows the test data set, comprising approximately 1500 structures. The species are color-coded as follows: blue, H_2COO ; orange, $HCO + OH$; green, cyc- H_2CO_2 ; red, OCH_2O ; purple, $HCOOH$; brown, $CO_2 + H_2$; and gray, $H_2O + CO$. The inset displays the training data set, which contains approximately 12000 structures. The coefficients of determination are $R^2 = 0.9984$ for the test set and $R^2 = 0.9983$ for the training set. The black solid line denotes the ideal 1:1 correlation.

S1.2 MD Simulations

All production MD simulations were carried out using the pyCHARMM software package^{38–40} in combination with interfaces to PhysNet.^{41,42} A time step of $\Delta t = 0.1$ fs was employed throughout the simulations. The initial conditions for all trajectories were prepared from a 1 ns equilibrium *NVE* simulation, following heating of H₂COO to 300 K over 200 ps and subsequent equilibration for 50 ps.^{20,21} From a set of 10 independent simulations, coordinates and velocities were recorded every 100 fs, yielding a total of 10⁶ structures to serve as starting points for the non-equilibrium dynamics. Each trajectory was propagated up to a maximum simulation time of 1 ns or they were terminated once dissociation into molecular products had occurred. To assign individual MD snapshots to specific states along the reaction pathway (Figure 1), a set of geometric criteria was applied, summarized in Table S1.

Table S1: Geometrical criteria were used to assign structures along the trajectories. Distances and angles are reported in units of Å and °, respectively. For the two C–H and C–O bond lengths, as well as the two possible C–O–O angles, the criteria were applied twice when necessary. The abbreviation “n.u.” denotes “not used.”

Species	H ₂ COO	cyc-H ₂ CO ₂	OCH ₂ O	HCOOH
distance CH	< 1.8	< 1.5	< 1.5	< 1.5, > 1.5
distance CO	< 1.8, > 1.7	< 2.0	< 2.0	< 1.6, < 1.8
distance OO	< 2.3	n.u.	n.u.	> 2.0
angle COO	> 90, < 90	< 90	< 90	< 90
angle OCO	< 90	< 95	≥ 95	> 90

The reactive dynamics was initiated by selectively exciting a combination mode corresponding to 3 quanta in the CH-stretch ($3\nu_{\text{CH}}$) and 1 quantum in the COO bending mode ($1\nu_{\text{COO}}$), resulting in a total vibrational energy of 25.5 kcal/mol. This targeted vibrational excitation allows the system to access the reactive regions of the PES efficiently and facilitates barrier crossing toward product formation. Excitations closer to the TS1-barrier energy lead to the same three dissociation products (CO₂ + H₂, H₂O + CO, and HCO + OH), but the reactions occur on significantly longer timescales.²⁰

Analysis of the fragment energies followed an established energy partitioning scheme akin to that described earlier in the literature.⁴³ For this, the total kinetic energy was computed as the sum of atomic kinetic energies. Product fragments were identified from the final atomic configuration, and for each fragment the center-of-mass (CoM) velocity was obtained from mass-weighted atomic velocities. The translational kinetic energy of each fragment was defined as $E_{\text{trans}} = \frac{1}{2}MV_{\text{CoM}}^2$ where M is the mass of the fragment, corresponding to three translational degrees of freedom. After removing the CoM motion, the internal kinetic energy $E_{\text{int}} = E_{\text{tot}} - E_{\text{trans}}$ was evaluated using velocities relative to the fragment CoM.

The instantaneous angular momentum was computed as $\mathbf{L} = \sum_i m_i (\mathbf{r}_i - \mathbf{r}_{\text{CoM}}) \times (\mathbf{v}_i - \mathbf{v}_{\text{CoM}})$ and the moment-of-inertia tensor as $\mathbf{I} = \sum_i m_i \left[|\mathbf{r}_i - \mathbf{r}_{\text{COM}}|^2 \mathbf{1} - (\mathbf{r}_i - \mathbf{r}_{\text{CoM}}) (\mathbf{r}_i - \mathbf{r}_{\text{CoM}})^T \right]$. From this, the angular velocity $\boldsymbol{\omega}$ was obtained by solving $\mathbf{I}\boldsymbol{\omega} = \mathbf{L}$ and the rotational kinetic energy was computed as $E_{\text{rot}} = \frac{1}{2} \sum_i m_i |\boldsymbol{\omega} \times (\mathbf{r}_i - \mathbf{r}_{\text{COM}})|^2$ corresponding to two rotational degrees of freedom for linear fragments and three for nonlinear fragments. Finally, the vibrational kinetic energy was obtained from $E_{\text{vib}} = E_{\text{int}} - E_{\text{rot}}$ where the internal kinetic energy is given by $E_{\text{int}} = \frac{1}{2} \sum_i m_i |\mathbf{v}_i - \mathbf{v}_{\text{CoM}}|^2$. The vibrational term accounts for the remaining $3N - 5$ (linear fragments) or $3N - 6$ (nonlinear fragments) degrees of freedom.

S1.3 Product State PESs

For H₂, CO, and OH, the energy profiles as functions of bond length are only modestly perturbed as the distance to the triatomic partner changes, see Figure S2. This indicates that the intramolecular bond dynamics of the diatomic products are largely decoupled from the translational separation of the fragments, especially at larger separations. The angle between the diatomic and the triatomic is fixed at 100°. At large fragment separations (~ 5 Å, corresponding to the blue curves in Figure S2), the interaction effectively terminates,

and the energy profiles approach those of the isolated diatomic species. Different colors represent different distances between the diatomic and triatomic fragments, highlighting how the interaction energy changes with separation. In the asymptotic limit, a crossing appears for the $\text{HCO} + \text{OH}$ channel. However, this feature occurs at energies well above the initial energy of the simulations (approximately 25.5 kcal/mol) and therefore does not influence the MD trajectories, considering that the initial energy of simulation is around 25.5 kcal/mol.

Figures S3 to S5 illustrate the PESs of the triatomic products CO_2 , H_2O , and HCO in the presence of their corresponding diatomic partners, H_2 , CO , and OH , respectively. The two CO bond lengths in CO_2 are varied around their equilibrium value. At short diatomic-triatomic distance, as the upper left panel shows, the energy profile of two CO bond stretching is not symmetric, since the interaction between CO_2 and H_2 is not symmetric, see Figure S2. The close agreement between the C–O dissociation energy shown in this figure (approximately 130 kcal/mol) and the experimentally reported value of 126 kcal/mol²² supports the reliability of the present PES. For $\text{CO}_2 + \text{H}_2$, the CO bonds remain intact because dissociation requires much higher energy and in the MD trajectories some energy is carried away by H_2 , making CO bond cleavage unlikely.

For the $\text{H}_2\text{O} + \text{CO}$ system, variations in the OH bond lengths are similarly explored across different H_2O –CO separations, revealing a stable triatomic product region under the simulation conditions.

For $\text{HCO} + \text{OH}$, the potential energy minimum rises with increasing HCO –OH separation, reflecting the barrierless nature of HCOOH decomposition. The CH bond dissociation energy of approximately 15 kcal/mol is below the total initial energy of the simulation, allowing a subset of trajectories to access the $\text{H} + \text{CO} + \text{OH}$ channel. The CH and CO bond lengths in HCO are varied around their equilibrium value. At a separation of 5 Å, the

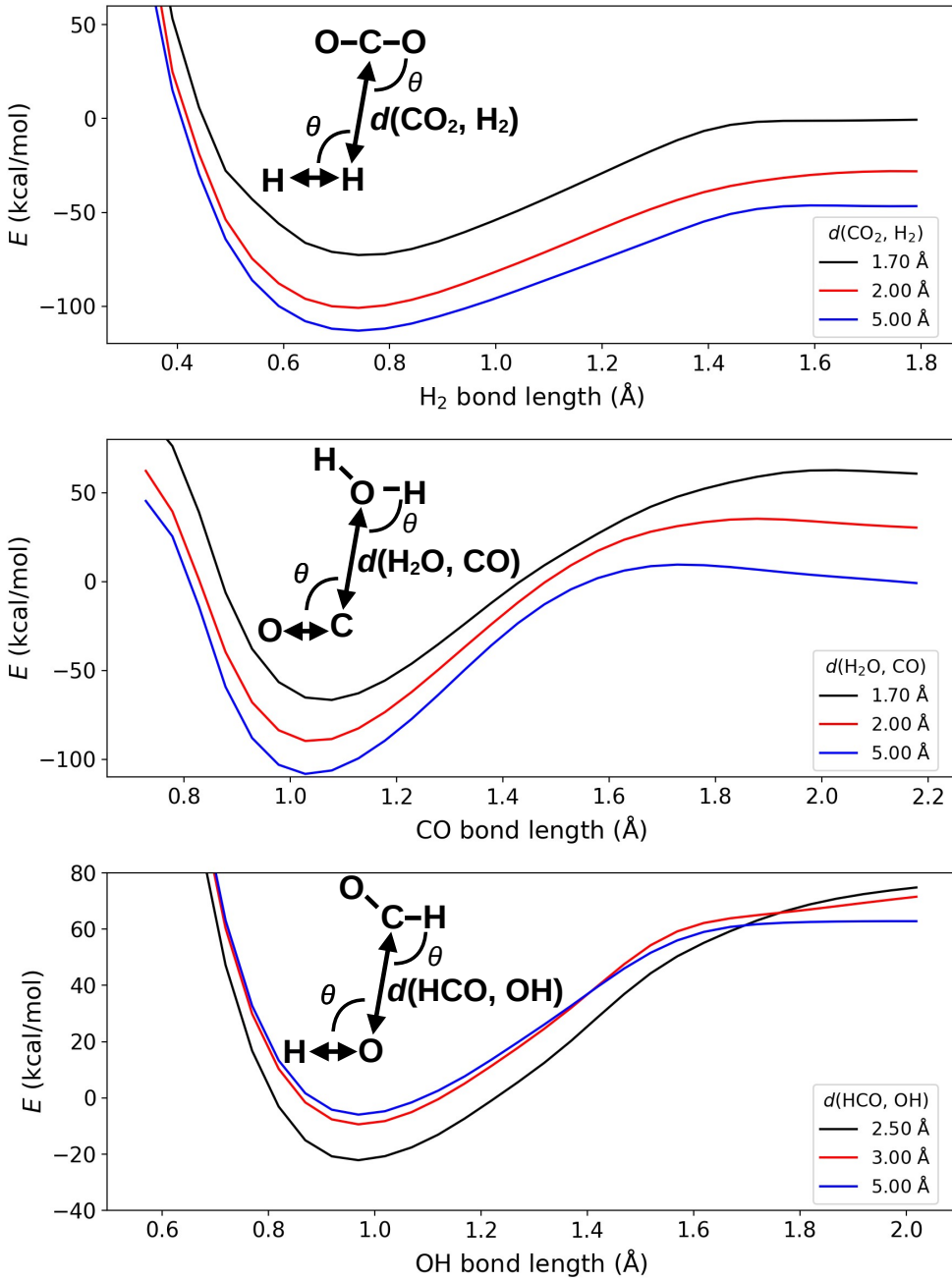


Figure S2: The energy profile of the diatomic products, i.e., H_2 (upper panel), CO (middle panel), and OH (lower panel). For each species, the diatom and the corresponding triatomic molecule were placed at three different distances, as indicated by the different colors in this figure. All the values of angle θ are fixed at 100°. The structures of the triatomic molecules were fixed at their equilibrium structure, while the bond length in the diatomic was scanned around its equilibrium value.

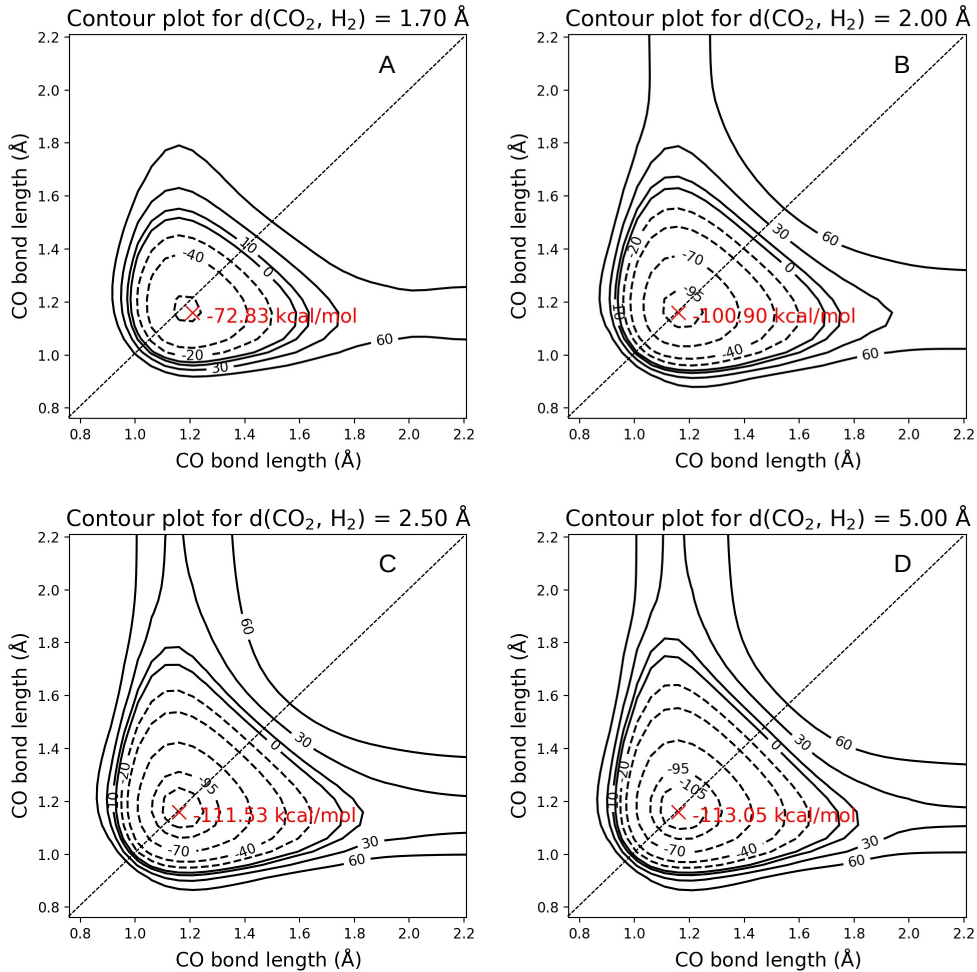


Figure S3: The PES $V(r_{\text{CO}_A}, r_{\text{CO}_B})$ of the CO_2 product with the partner diatomic fragment H_2 was fixed at its equilibrium bond length of 0.741 Å whereas the CO_2 molecule was constrained to remain linear. In each panel, a specific CO_2 – H_2 separation is examined. The definition of this distance and the position of H_2 relative to CO_2 are presented in the upper panel of Figure S2.

HCO molecule should behave essentially as a free HCO radical. The CH bond dissociation energy is ~ 15 kcal/mol, in good agreement with previous studies reporting values of 13.36 kcal/mol²³ and 14.40 kcal/mol.²⁴ In addition, along the H-atom dissociation pathway, a transition state is observed in this figure. This transition state was also identified in earlier MRCI/aug-cc-pVQZ²³ and CCSD(T)/CBS//CCSD/aug-cc-pVTZ²⁴ studies and lies below the initial 25.5 kcal/mol of energy available in the MD simulations. As a result, a small fraction of trajectories proceeded to form the $\text{H} + \text{CO} + \text{OH}$ products. The minimum

rises with increasing $d(\text{HCO}, \text{OH})$, in contrast to the $\text{CO}_2 + \text{H}_2$ and $\text{H}_2\text{O} + \text{CO}$ cases. This behavior is expected, as HCOOH decomposition proceeds without a transition state. The potential energy rises as the HCO and OH separation grows. These energy profiles collectively demonstrate how the interaction between triatomic products and their diatomic partners shapes the accessible reaction pathways in the MD simulations.

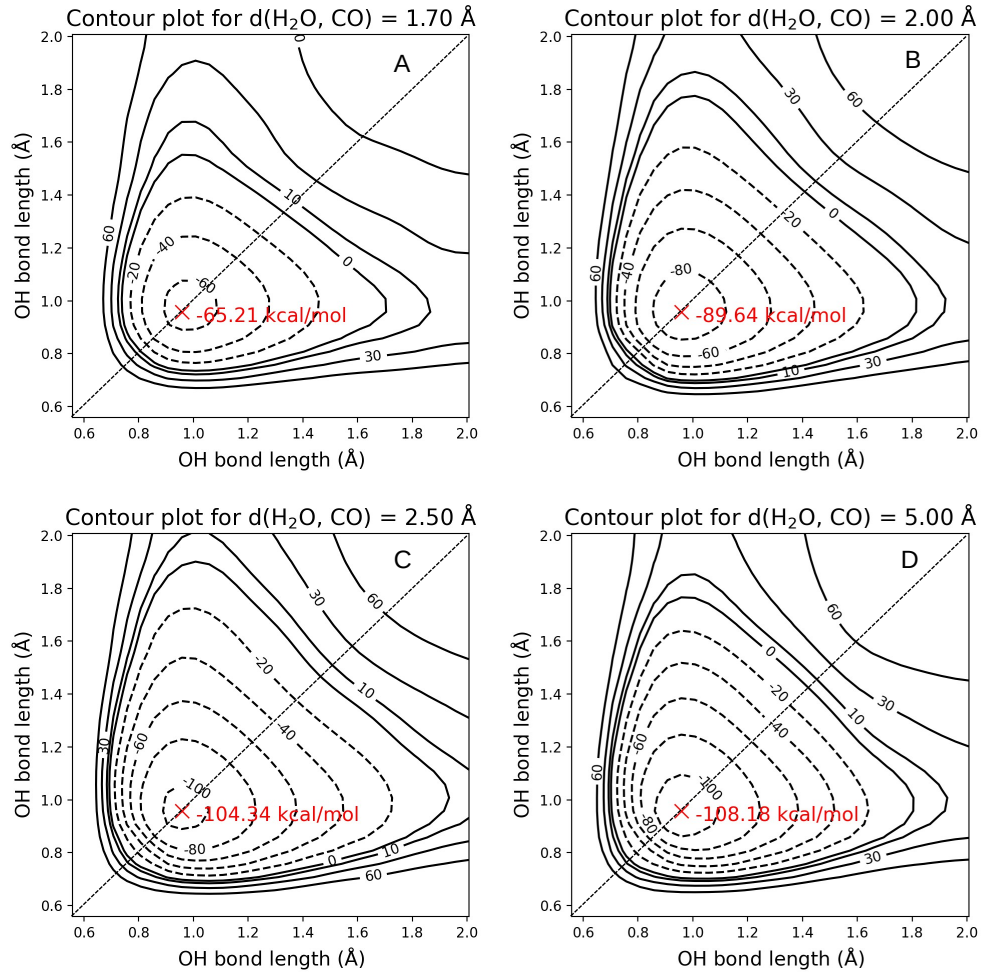


Figure S4: The PES $V(r_{\text{OH}_A}, r_{\text{OH}_B})$ of the triatomic product H_2O was evaluated while the partner diatomic fragment CO was fixed at its equilibrium bond length of 1.128 \AA . The HOH angle in H_2O molecule was constrained to 104.5° . In each panel, a certain $\text{H}_2\text{O}-\text{CO}$ separation distance is examined. The precise definition of this distance and the position of CO relative to H_2O are presented in the middle panel of Figure S2. The two OH bond lengths in H_2O are varied around their equilibrium value.

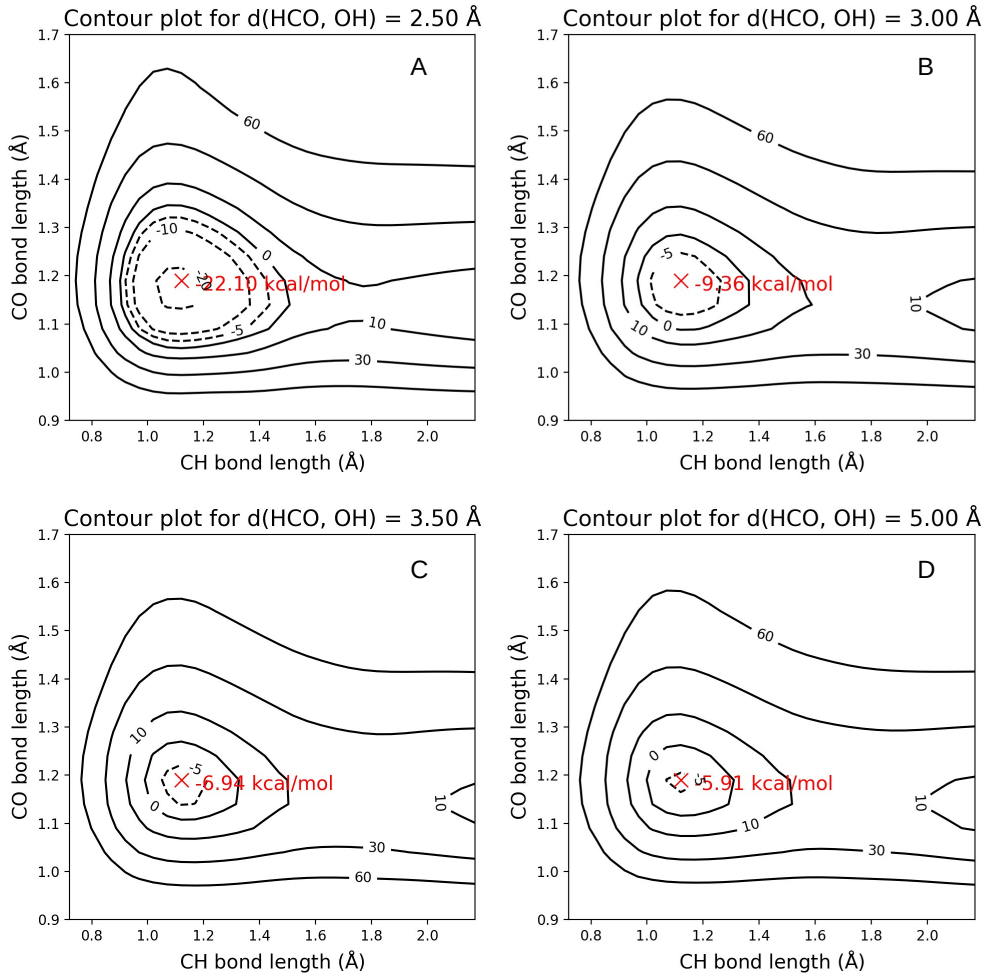


Figure S5: The PES $V(r_{\text{CH}}, r_{\text{CO}})$ of the triatomic product HCO with the diatomic fragment OH fixed at its equilibrium bond length of 0.969 Å. The H-C-O angle for HCO was constrained to 124°. In each panel, a HCO–OH separations ranging from 2.5 Å to 5.0 Å are examined, see the lower panel of Figure S2.

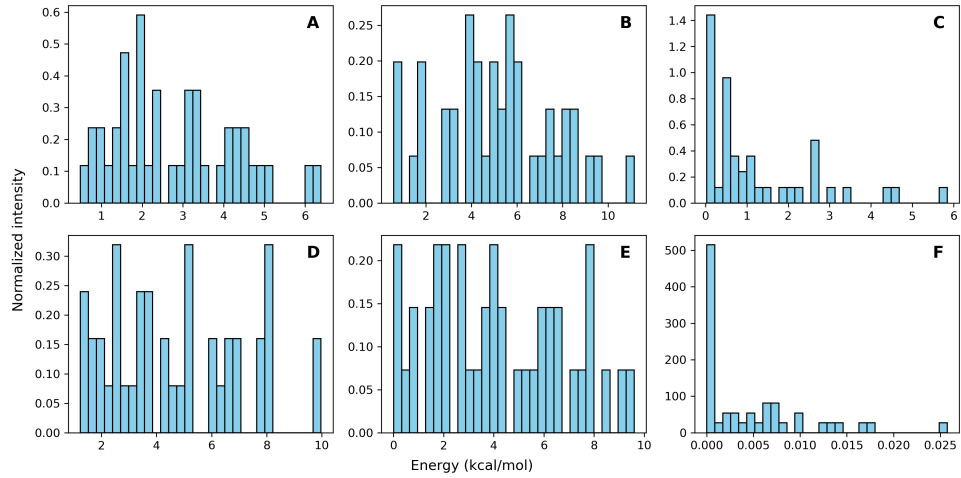


Figure S6: Energy distributions of the product $\text{HCO}+\text{OH}$ from 40 simulations. The top panels show fragment HCO and bottom show fragment OH . From left to right, the distributions correspond to translational, translational, rotational, and vibrational energies. Because only 40 trajectories produce this product, the data are not sufficient to yield a converged energy distribution, as was achieved for CO_2+H_2 and $\text{H}_2\text{O}+\text{CO}$.

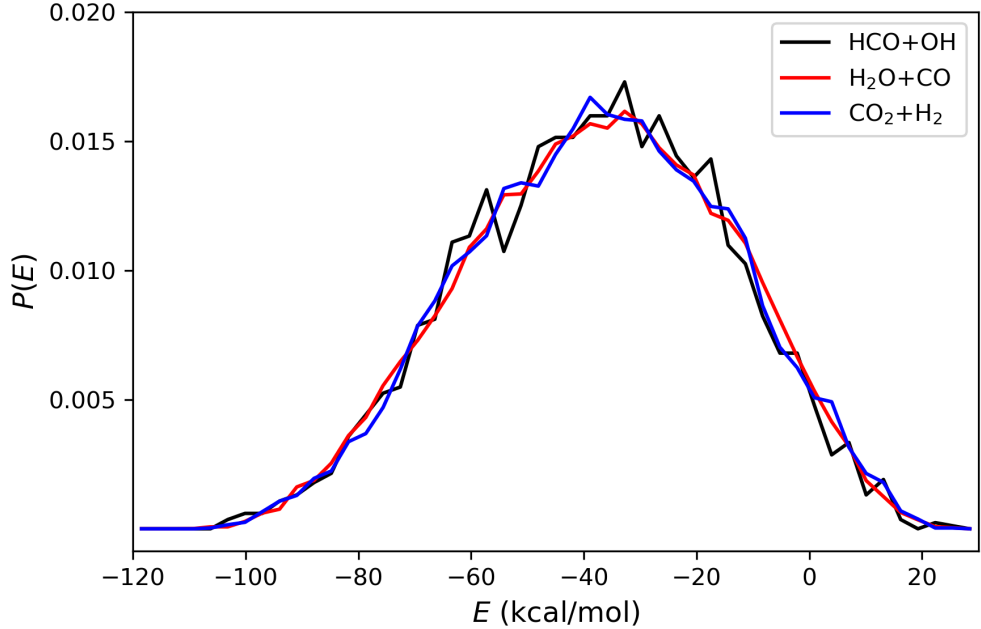


Figure S7: The energy distributions of HCOOH associated with the three product channels, $\text{HCO}+\text{OH}$ (black), $\text{H}_2\text{O}+\text{CO}$ (red), and CO_2+H_2 (blue). The peak is located at ~ -40 kcal/mol, whereas the potential energy of equilibrium HCOOH is around -140 kcal/mol. This indicates that during the simulation HCOOH possesses ~ 100 kcal/mol of internal energy.

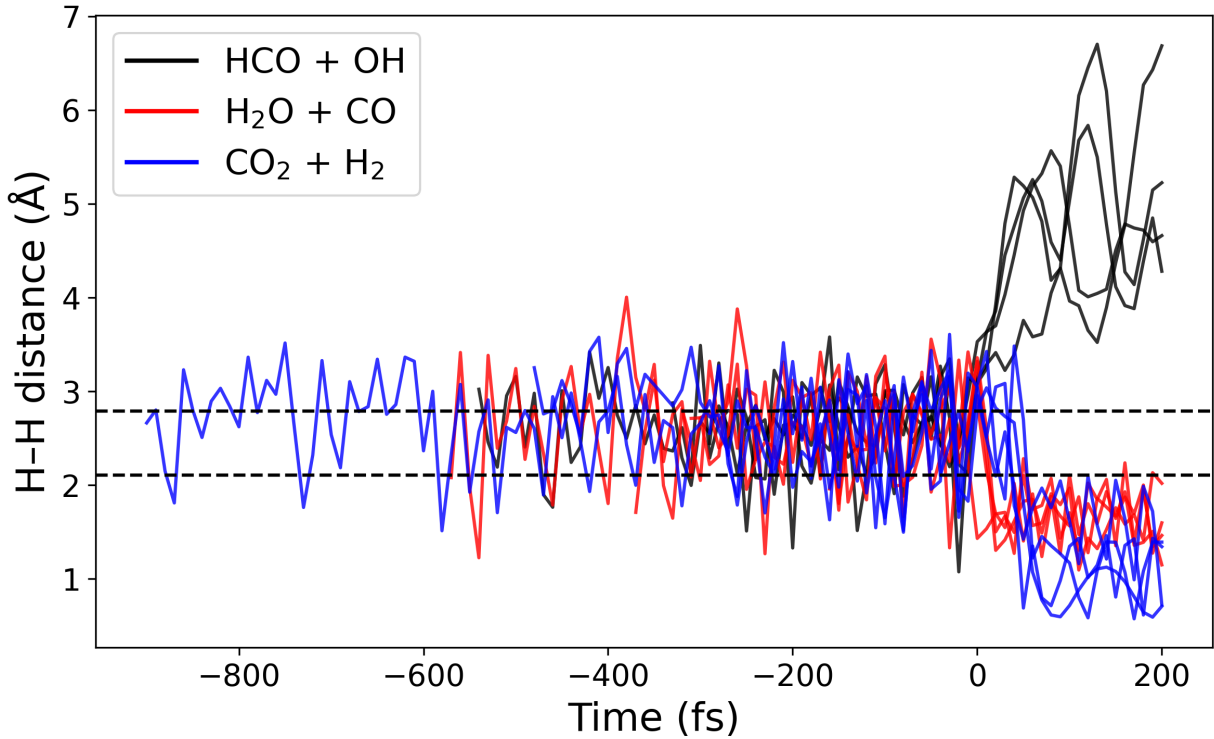


Figure S8: Time evolution of the H–H separation along reactive molecular dynamics trajectories leading to three different product channels. Trajectories forming $\text{HCO} + \text{OH}$ are shown in black, $\text{H}_2\text{O} + \text{CO}$ in red, and $\text{CO}_2 + \text{H}_2$ in blue, with four representative trajectories shown for each channel. The time axis is shifted such that $t = 0$ corresponds to the frame of product formation; negative times indicate configurations in the HCOOH region, while positive times correspond to the product region. The two dashed lines indicate the H–H separation in the equilibrium structures of *cis*- and *trans*- HCOOH , respectively.

References

(1) Criegee, R.; Wenner, G. Die Ozonisierung des 9, 10-Oktalins. *Justus Liebigs Ann. Chem.* **1949**, *564*, 9–15.

(2) Nguyen, T. L.; Lee, H.; Matthews, D. A.; McCarthy, M. C.; Stanton, J. F. Stabilization of the simplest Criegee intermediate from the reaction between ozone and ethylene: A high-level quantum chemical and kinetic analysis of ozonolysis. *J. Phys. Chem. A* **2015**, *119*, 5524–5533.

(3) Green, A. M.; Barber, V. P.; Fang, Y.; Klippenstein, S. J.; Lester, M. I. Selective deuteration illuminates the importance of tunneling in the unimolecular decay of Criegee intermediates to hydroxyl radical products. *Proc. Natl. Acad. Sci. USA* **2017**, *114*, 12372–12377.

(4) Yin, C.; Takahashi, K. How does substitution affect the unimolecular reaction rates of Criegee intermediates? *Phys. Chem. Chem. Phys.* **2017**, *19*, 12075–12084.

(5) Vereecken, L.; Novelli, A.; Taraborrelli, D. Unimolecular decay strongly limits the atmospheric impact of Criegee intermediates. *Phys. Chem. Chem. Phys.* **2017**, *19*, 31599–31612.

(6) Stone, D.; Blitz, M.; Daubney, L.; Howes, N. U.; Seakins, P. Kinetics of CH_2OO reactions with SO_2 , NO_2 , NO , H_2O and CH_3CHO as a function of pressure. *Phys. Chem. Chem. Phys.* **2014**, *16*, 1139–1149.

(7) Qiu, J.; Tonokura, K. Detection of the simplest Criegee intermediate CH_2OO in the $\nu 4$ band using a continuous wave quantum cascade laser and its kinetics with SO_2 and NO_2 . *Chem. Phys. Lett.* **2019**, *737*, 100019.

(8) Yin, C.; Czakó, G. Revealing new pathways for the reaction of Criegee intermediate CH_2OO with SO_2 . *Comm. Chem.* **2024**, *7*, 157.

(9) Chao, W.; Hsieh, J.-T.; Chang, C.-H.; Lin, J. J.-M. Direct kinetic measurement of the reaction of the simplest Criegee intermediate with water vapor. *Science* **2015**, *347*, 751–754.

(10) Yin, C.; Takahashi, K. Effect of unsaturated substituents in the reaction of Criegee intermediates with water vapor. *Phys. Chem. Chem. Phys.* **2018**, *20*, 20217–20227.

(11) Vereecken, L.; Francisco, J. S. Theoretical studies of atmospheric reaction mechanisms in the troposphere. *Chem. Soc. Rev.* **2012**, *41*, 6259–6293.

(12) Berndt, T.; Jokinen, T.; Sipilä, M.; Mauldin, R. L.; Herrmann, H.; Stratmann, F.; Junninen, H.; Kulmala, M. Gas-Phase Ozonolysis of Selected Olefins: The Yield of Stabilized Criegee Intermediate and the Reactivity toward SO₂. *Science* **2012**, *335*, 204–208.

(13) Welz, O.; Savee, J. D.; Osborn, D. L.; Vasu, S. S.; Percival, C. J.; Shallcross, D. E.; Taatjes, C. A. Direct kinetic measurements of Criegee intermediate (CH₂OO) formed by reaction of CH₂I with O₂. *Science* **2012**, *335*, 204–207.

(14) Taatjes, C. A. Criegee intermediates: What direct production and detection can teach us about reactions of carbonyl oxides. *Ann. Rev. Phys. Chem.* **2013**, *64*, 387–410.

(15) Fang, Y.; Liu, F.; Barber, V. P.; Klippenstein, S. J.; McCoy, A. B.; Lester, M. I. Communication: Real time observation of unimolecular decay of Criegee intermediates to OH radical products. *J. Chem. Phys.* **2016**, *144*, 061102.

(16) Fang, Y.; Liu, F.; Barber, V. P.; Klippenstein, S. J.; McCoy, A. B.; Lester, M. I. Deep tunneling in the unimolecular decay of CH₃CHOO Criegee intermediates to OH radical products. *J. Chem. Phys.* **2016**, *145*, 234308.

(17) Upadhyay, M.; Meuwly, M. Thermal and vibrationally activated decomposition of the syn-CH₃CHOO Criegee Intermediate. *ACS Earth Space Chem.* **2021**, *5*, 3396–3406.

(18) Upadhyay, M.; Toöpfer, K.; Meuwly, M. Molecular Simulation for Atmospheric Reactions: Non-Equilibrium Dynamics, Roaming, and Glycolaldehyde Formation following Photoinduced Decomposition of syn-Acetaldehyde Oxide. *J. Phys. Chem. Lett.* **15**, 90–96.

(19) Kidwell, N. M.; Li, H.; Wang, X.; Bowman, J. M.; Lester, M. I. Unimolecular dissociation dynamics of vibrationally activated CH_3CHOO Criegee intermediates to OH radical products. *Nat. Chem.* **2016**, *8*, 509–514.

(20) Yin, C.; Käser, S.; Upadhyay, M.; Meuwly, M. Photodissociation dynamics of energized H_2COO : Formation of molecular products. *J. Chem. Phys.* **2025**, *163*, 214305.

(21) Song, K.; Upadhyay, M.; Meuwly, M. OH-Formation following vibrationally induced reaction dynamics of H_2COO . *Phys. Chem. Chem. Phys.* **2024**, *26*, 12698–12708.

(22) Gong, S.; Wang, P.; Mo, Y. Bond dissociation energy of CO_2 with spectroscopic accuracy using state-to-state resolved threshold fragment yield spectra. *J. Phys. Chem. Lett.* **2024**, *15*, 10842–10848.

(23) Peters, P. S.; Duflot, D.; Wiesenfeld, L.; Toubin, C. The $\text{H} + \text{CO} \leftrightarrow \text{HCO}$ reaction studied by ab initio benchmark calculations. *J. Chem. Phys.* **2013**, *139*.

(24) Vichiotti, R. M.; Machado, F. B.; Haiduke, R. L. Accurate rate constants for the forward and reverse $\text{H} + \text{CO} \leftrightarrow \text{HCO}$ reactions at the high-pressure limit. *ACS omega* **2020**, *5*, 23975–23982.

(25) Sun, G.; Qin, Y.; Zheng, X.; Song, Y.; Zhang, J. Photodissociation of HCO Radical via the \tilde{A}^2A'' State: Accurate Determination of Bond Dissociation Energy $D_0(\text{H}-\text{CO})$. *Chin. J. Chem. Phys.* **2024**, *37*, 857–862.

(26) Qian, Y.; Nguyen, T. L.; Franke, P. R.; Stanton, J. F.; Lester, M. I. Nonstatistical

Unimolecular Decay of the CH₂OO Criegee Intermediate in the Tunneling Regime. *J. Phys. Chem. Lett.* **2024**, *15*, 6222–6229.

- (27) Kohlrausch, R. Theorie des elektrischen Rückstandes in der Leidener Flasche. *Annalen der Physik und Chemie* **1854**, *91*, 179–214.
- (28) Williams, G.; Watts, D. C. Non-symmetrical dielectric relaxation behaviour arising from a simple empirical decay function. *Transactions of the Faraday Society* **1970**, *66*, 80–85.
- (29) Austin, R. H.; Beeson, K. W.; Eisenstein, L.; Frauenfelder, H.; Gunsalus, I. C. Dynamics of Ligand Binding to Myoglobin. *Phys. Rev. Lett.* **1974**, *32*, 403–405.
- (30) Austin, R.; Beeson, K.; Eisenstein, L.; Frauenfelder, H.; Gunsalus, I. Dynamics of ligand binding to myoglobin. *Biochemistry* **1975**, *14*, 5355–5373.
- (31) Richert, R. Heterogeneous dynamics in liquids: fluctuations in space and time. *Journal of Physics: Condensed Matter* **2002**, *14*, R703–R738.
- (32) Yu, Y.; Wang, M.; Zhang, D.; Bauchy, M. Stretched exponential relaxation of glasses at low temperature. *Phys. Rev. Lett.* **2015**, *115*, 165901.
- (33) Frauenfelder, H.; Sligar, S. G.; Wolynes, P. G. The energy landscapes and motions of proteins. *Science* **1991**, *254*, 1598–1603.
- (34) Soloviov, M.; Das, A. K.; Meuwly, M. Structural Interpretation of Metastable States in Myoglobin–NO. *Angew. Chem. Int. Ed.* **2016**, *55*, 10126–10130.
- (35) Pezzella, M.; Meuwly, M. O₂ formation in cold environments. *Phys. Chem. Chem. Phys.* **2019**, *21*, 5559–5571.
- (36) Werner, H.-J.; Knowles, P. J.; Manby, F. R.; Black, J. A.; Doll, K.; Hesselmann, A.; Kats, D.; Koehn, A.; Korona, T.; Kreplin, D. A. et al. The Molpro quantum chemistry package. *J. Chem. Phys.* **2020**, *152*, 144107.

(37) Unke, O. T.; Meuwly, M. PhysNet: A Neural Network for Predicting Energies, Forces, Dipole Moments, and Partial Charges. *J. Chem. Theory Comput.* **2019**, *15*, 3678–3693.

(38) Brooks, B. R.; Brooks III, C. L.; Mackerell Jr, A. D.; Nilsson, L.; Petrella, R. J.; Roux, B.; Won, Y.; Archontis, G.; Bartels, C.; Boresch, S. et al. CHARMM: the biomolecular simulation program. *J. Comput. Chem.* **2009**, *30*, 1545–1614.

(39) Buckner, J.; Liu, X.; Chakravorty, A.; Wu, Y.; Cervantes, L. F.; Lai, T. T.; Brooks III, C. L. pyCHARMM: embedding CHARMM functionality in a python framework. *J. Chem. Theory Comput.* **2023**, *19*, 3752–3762.

(40) Hwang, W.; Austin, S. L.; Blondel, A.; Boittier, E. D.; Boresch, S.; Buck, M.; Buckner, J.; Caflisch, A.; Chang, H.; Cheng, X. et al. CHARMM at 45: Enhancements in Accessibility, Functionality, and Speed. *J. Phys. Chem. B* **2024**, *128*, 9976–10042.

(41) Song, K.; Käser, S.; Töpfer, K.; Vazquez-Salazar, L. I.; Meuwly, M. PhysNet Meets CHARMM: A Framework for Routine Machine Learning/Molecular Mechanics Simulations. *J. Chem. Phys.* **2023**, *159*, 024125.

(42) Töpfer, K.; Vázquez-Salazar, L. I.; Meuwly, M. Asparagus: A Toolkit for Autonomous, User-Guided Construction of Machine-Learned Potential Energy Surfaces. *Comp. Phys. Comm.* **2025**, *308*, 109446.

(43) Hase, W. L. *Encyclopedia of Computational Chemistry*; Wiley, New York, 1998; pp 399–407.